J Mater Sci (2019) 54:8236–8246

Chemical routes to materials

Synergetic effect of Fe_2O_3 and $BiVO_4$ as photocatalyst nanocomposites for improved photo-Fenton catalytic activity

Yun Wen[1], Yue Zhao[1], Mingzhen Guo[1], and Yan Xu[1,*]

[1] *Department of Chemistry, College of Science, Northeastern University, Shenyang 110819, Liaoning, China*

Received: 11 November 2018
Accepted: 4 March 2019
Published online: 8 March 2019

© Springer Science+Business Media, LLC, part of Springer Nature 2019

ABSTRACT

Photo-Fenton reactions and the related functional nanomaterials have been widely studied for applications in wastewater treatment industry. Herein, visible-light-responsive Fe_2O_3 nanoparticle-decorated $BiVO_4$ nanoplates were designed and successfully prepared through a one-pot hydrothermal route. The as-prepared $Fe_2O_3/BiVO_4$ nanocomposites exhibit excellent photo-Fenton catalytic activity toward the discoloration of methylene blue (MB) and Rhodamine B (RhB) dye molecules in the presence of H_2O_2. The experimental results indicate that nearly 100% of MB (100 mL, 10 mg L^{-1}) and RhB (100 mL, 5 mg L^{-1}) dye molecules are degraded in the presence of 1 g L^{-1} $Fe_2O_3/BiVO_4$-1 (FB-1) photo-Fenton catalyst and 0.5 mL of H_2O_2 within 20 min. The $Fe_2O_3/BiVO_4$ Fenton photocatalyst also demonstrates high reusability under visible light irradiation with $\lambda \geq 420$ nm. The photoinduced electrons on the conduction band of $BiVO_4$ nanoplates can move toward the surface of $Fe_2O_3/BiVO_4$ to accelerate the reduction of Fe^{3+}; then, the as-formed Fe^{2+} ions on the surface of the catalyst greatly enhance the decomposition of H_2O_2 to form reactive $^{\cdot}OH$ species for the use in photodegradation of MB and RhB dye molecules. The synergetic effect of Fe_2O_3 and $BiVO_4$ reported in this work might provide more opportunity to fabricate other novel semiconductor-based Fenton nanocomposites for contamination treatments in wastewater.

Introduction

Recently, photo-Fenton reactions involving hydrogen peroxide (H_2O_2) and Fe^{2+} ions to produce highly reactive oxygen species (generally $^{\cdot}OH$), as well as the related materials themselves, have been widely used in wastewater treatment industry to decompose various organic pollutants [1–3]. However, the utilization of large amount of iron inorganic salts in the treated wastewater might bring about the production of Fe-containing sludge in which Fe ions are difficult to be recycled. Moreover, most of the Fenton reaction systems must be performed under acidic medium [3]. These shortcomings greatly inhibit the application of

Address correspondence to E-mail: xuyanjlu@126.com

https://doi.org/10.1007/s10853-019-03511-x

the photo-Fenton catalytic technology even though it has the characteristics of easier operation and fast reaction rate. Thus, developing new photo-Fenton catalysts with high chemical oxidant of $^{\cdot}OH$ generation efficiency, expanded acidity effective range, and multiple recyclability is of great significance.

In addition, fast chemical reduction of Fe^{3+} ions to Fe^{2+} either in aqueous solution or on the surface of catalysts is expected to be a facile route to promote the Fenton catalytic performance [4, 5]. Previous investigations have demonstrated that the introduction of UV or visible-light-responsive photocatalyst with large amounts of excited electrons is a promising strategy [6–8], which can reduce Fe^{3+} ions to Fe^{2+} in a quick way under a nearly neutral condition and further accelerate the photo-Fenton procedure. Meanwhile, the photocatalysts as the additional platform for photo-Fenton reactions can be shaped into different morphologies, including nanotubes, nanowires, nanobelts, and nanoplates [9–12]. These nanosized catalysts usually had superior photocatalytic activities than those of the bulk materials due to their large surface area and stronger light absorption capacity [13]. Notably, the nanoplates featuring ultrathin thickness and high structural anisotropy have been paid an increasing attention to be used as the platform materials [14]. Hydrothermal method is regarded as a simple pathway toward morphology-controlled synthesis of nanoplates [15].

In this work, a feasible one-pot hydrothermal synthetic route was carried out to construct Fe_2O_3 nanoparticle-decorated $BiVO_4$ photo-Fenton system in $FeCl_3$–$Bi(NO_3)_3$–NH_4VO_3 aqueous solution. As is known to all, bismuth vanadate ($BiVO_4$), as visible-light-responsive photocatalysts, possessed relatively narrow band gap energy (< 2.5 eV) and high photocatalytic activity in the evolution of H_2 and O_2, as well as degradation of organic contaminants [16, 17]. Therefore, $BiVO_4$ is considered to be one of the most promising candidates to fabricate novel photo-Fenton system [18]. Under light irradiation, the photogenerated electrons in the conduction band of $BiVO_4$ nanoplates are transferred to the surface to enhance the chemical reduction of Fe^{3+} to Fe^{2+} ions, and as-formed redundant Fe^{2+} then reacts with H_2O_2 to accelerate its decomposition into reactive $^{\cdot}OH$ species, which is further applied for the photodegradation of organic pollutant. Methylene blue (MB) and Rhodamine B (RhB) belong to two important basic dyes with *N*-methyl and *N*-ethyl groups in their molecular structures, respectively. They have been widely used in various industries for coloring and further cause plenty of disposal environmental problems. Thus, MB and RhB dye molecules are selected as the model pollutions to investigate the photocatalytic activity of Fe_2O_3-decorated $BiVO_4$ (denoted as $Fe_2O_3/BiVO_4$ nanocomposites) in the following study. The mechanism of the photo-Fenton catalytic process is also investigated through the corresponding verification experiments and discussed in detail.

Experimental

Materials

The starting materials include ferric chloride ($FeCl_3{\cdot}6H_2O$, 99.0%, Zhiyuan, Tianjin, China), bismuth nitrate pentahydrate ($Bi(NO_3)_3{\cdot}5H_2O$, 99.0%, Damao, Tianjin, China), ammonium metavanadate (NH_4VO_3, Aladdin, Shanghai, China), sodium hydroxide (NaOH, 99.5%, Guoyao, Shanghai, China), and distilled water. All of the reagents are analytical-grade regents and used as received without any purification.

Preparation of $Fe_2O_3/BiVO_4$ nanocomposites

The $Fe_2O_3/BiVO_4$ nanocomposites were prepared through a simple hydrothermal strategy in the $FeCl_3$–$Bi(NO_3)_3$–NH_4VO_3–H_2O synthetic system. Typically, a certain amount of $FeCl_3{\cdot}6H_2O$ (1–5 mmol) and $Bi(NO_3)_3{\cdot}5H_2O$ (5 mmol) was added into 60 mL of distilled water under magnetic stirring condition, and a yellow suspension was formed. Then, 5 mmol of NH_4VO_3 was added, and an orange suspension was formed. Then, the pH value of the mixture is adjusted to about 6.0 by using sodium hydroxide solution (5 M), which was then placed in a Teflon-lined autoclave with maximum volume of about 100 mL and heated at 160 °C for 12 h in an electric heating oven. The resultant yellow $Fe_2O_3/BiVO_4$ powder was collected, washed with distilled water and ethanol triple times, respectively, and dried at 60 °C for 2 h for further characterization. Samples of different molars of $FeCl_3{\cdot}6H_2O$ (1 mmol, 2 mmol, 3 mmol, 4 mmol, 5 mmol) were denoted as FB-1, FB-2, FB-3, FB-4, FB-5, respectively. Pure $BiVO_4$ was also

prepared by a similar procedure without the addition of $FeCl_3{\cdot}6H_2O$.

Characterization

The phase structures of the plate-like $BiVO_4$ and $Fe_2O_3/BiVO_4$ nanocomposites were investigated by powder X-ray diffraction performed on a X′Pert Pro MRDDY2094 diffractometer with Cu-Kα radiation (λ = 1.5418 Å). We recorded the XRD patterns of the samples in the 2θ range of 15°–80° under a scan rate of 0.0167 s^{-1}. The morphology of the plate-like $BiVO_4$ and $Fe_2O_3/BiVO_4$ nanocomposites was characterized by using the Ultra Plus field-emission scanning electron microscope (FE-SEM) accompanied with an energy-dispersive spectroscopy (EDS) to analyze the chemical composition. High-resolution transmission electron microscope (HRTEM) images were measured under the accelerating voltage of 200 kV on a JEOL JSM-2100F microscope. X-ray photoelectron spectroscopy (XPS) was conducted to identify the surface elemental composition. The UV–visible adsorption spectra of these samples were characterized using a Hitachi U-3100 UV–visible spectrometer. The photo-Fenton activities of $BiVO_4$ and $Fe_2O_3/BiVO_4$ nanocomposites were measured by monitoring the MB or RhB concentration at their maximum absorption with a UV–Vis spectrophotometer.

Photocatalytic properties

The dyes of Rhodamine B (RhB) and methylene blue (MB) were chosen as typical pollutants to evaluate the photo-Fenton catalytic performance of the $Fe_2O_3/BiVO_4$ nanocomposites. In detail, 0.1 g of the $Fe_2O_3/BiVO_4$ catalyst was introduced into a 100 mL of MB (10 mg L^{-1}) or RhB (5 mg L^{-1}) aqueous solution. The mixture was under continuous stirring for 30 min in the darkness to achieve the dye adsorption equilibrium. The degradation experiments were subsequently started at neutral aqueous solutions (pH 7) under a 300-W Xe lamp light irradiation with a cutoff filter (λ = 420–700 nm) at room temperature. A certain amount of H_2O_2 aqueous solution (30%) was injected into the above solution when the light irradiation began. Then, 3 mL of the treated solution was taken out at each time interval of 10 min and centrifuged at 9500 rpm for 5 min to remove the photocatalysts. The concentrations of MB or RhB dye molecules in the treated solution with maximum adsorption at about 554 nm and 664 nm were detected by UV–Vis spectrum, respectively. The recycling experiments of $Fe_2O_3/BiVO_4$ nanocomposites for degradation of the dye molecules were also performed in the same way, and the suspension was centrifuged with the catalysts recovered and used for the next run.

Results and discussion

Structure and morphology

The XRD patterns of pure $BiVO_4$ nanoplates, $Fe_2O_3/BiVO_4$ nanocomposites, and the simulated XRD pattern of $BiVO_4$ with JCPDS No. 75-1866 are shown in Fig. 1. It can be noticed that the as-prepared $BiVO_4$ nanoplates have the monoclinic structure of $BiVO_4$ (JCPDS No. 75-1866) as the main phase mixed with small amount of FeV_3O_8 phase (JCPDS No. 36-0007) as iron doping level increases [19, 20], which was marked with red asterisk. The peaks marked with blue asterisk are ascribed to Fe_2O_3 (JCPDS No. 85-0987) [21, 22], respectively. Also, the sharp and strong diffraction peaks illustrated the crystallinity of $Fe_2O_3/BiVO_4$ nanocomposites.

The morphologies of the $BiVO_4$ and $Fe_2O_3/BiVO_4$ nanocomposites were characterized by FE-SEM.

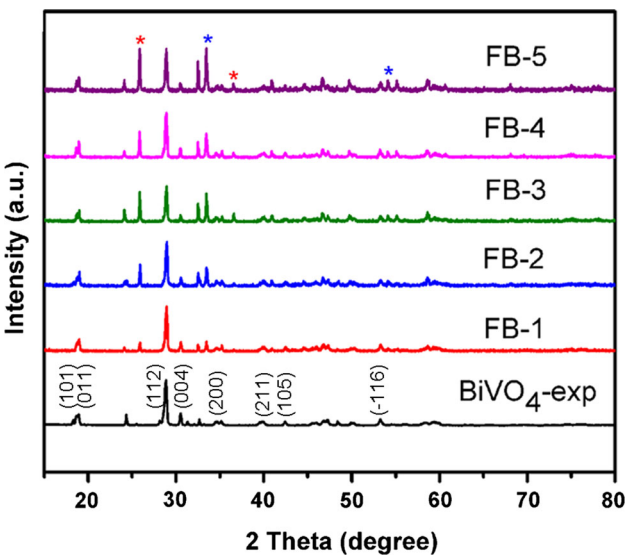

Figure 1 (From down to top) XRD patterns of plate-like $BiVO_4$ with JCPDS No. 75-1866, $Fe_2O_3/BiVO_4$ nanocomposites named as FB-1, FB-2, FB-3, FB-4, and FB-5, respectively. (Red asterisk, FeV_3O_8 with JCPDS No. 36-0007; blue asterisk, Fe_2O_3 with JCPDS No. 85-0987).

Figure 2a shows the irregular morphology of plate-like $BiVO_4$ samples. The SEM images of the Fe_2O_3/$BiVO_4$ nanocomposites by introducing different amounts of $FeCl_3{\cdot}6H_2O$ are shown in Fig. 2b–f, which are different from the pure $BiVO_4$ nanoplates, and large amounts of Fe_2O_3 nanoparticles appeared on the surface of the plates. Furthermore, as the doping level of Fe^{3+} ions increases in the synthetic system, the Fe_2O_3 nanoparticles aggregated together and formed a thin Fe_2O_3 layer over the surface of $BiVO_4$ nanoplates. In addition, the high-resolution transmission electron microscope images (HRTEM) of FB-1 are shown in Fig. 3a, b, in which the darker nanoparticles and the lighter plates correspond to Fe_2O_3 nanoparticles and $BiVO_4$, respectively. The lattices of $BiVO_4$ and Fe_2O_3 can also be clearly seen in Fig. 3b, suggesting the high crystallinity of Fe_2O_3/$BiVO_4$ composites. The selected SEM image and the corresponding overlapped elemental mapping image of FB-1 are shown in Fig. 3c and d, respectively. It can be observed that the elements of Fe (Red), Bi (Green), V (Blue), and O (Yellow) are coexisted in FB-1, indicating that these elements are all included in the final composite.

XPS, UV–Vis, and PL spectra

The XPS spectrum was measured to identify the surface chemical composition of Fe_2O_3/$BiVO_4$ nanocomposites. As shown in Fig. 4a, the XPS survey spectrum of FB-1 also demonstrates the coexistence of the elements including Fe, Bi, V, and O, which is in consistency with the result of EDS measurement. The high-resolution XPS spectrum of Fe 2*p* shows the two main peaks of Fe $2p_{1/2}$ and Fe $2p_{3/2}$ at 724.3 and 710.9 eV, respectively. A satellite peak of Fe $2p_{3/2}$ demonstrated the existence of Fe^{3+} in Fe_2O_3/$BiVO_4$ nanocomposites (Fig. 4b) [23]. In Fig. 4c, the peaks with binding energies of 159.2 and 164.5 eV corresponded to the Bi $4f_{7/2}$ and Bi $4f_{5/2}$ in FB-1,

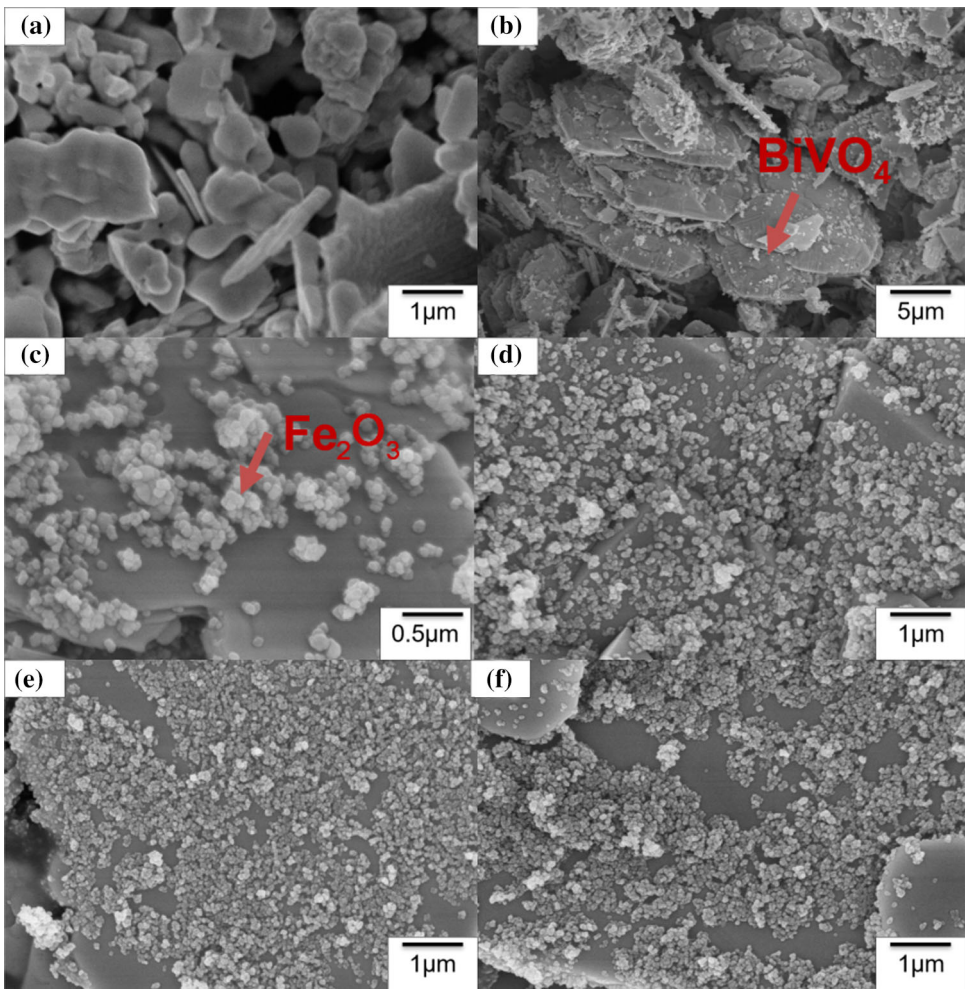

Figure 2 SEM images of **a** pure $BiVO_4$ nanoplates, **b** FB-1, **c** FB-2, **d** FB-3, **e** FB-4, and **f** FB-5, respectively.

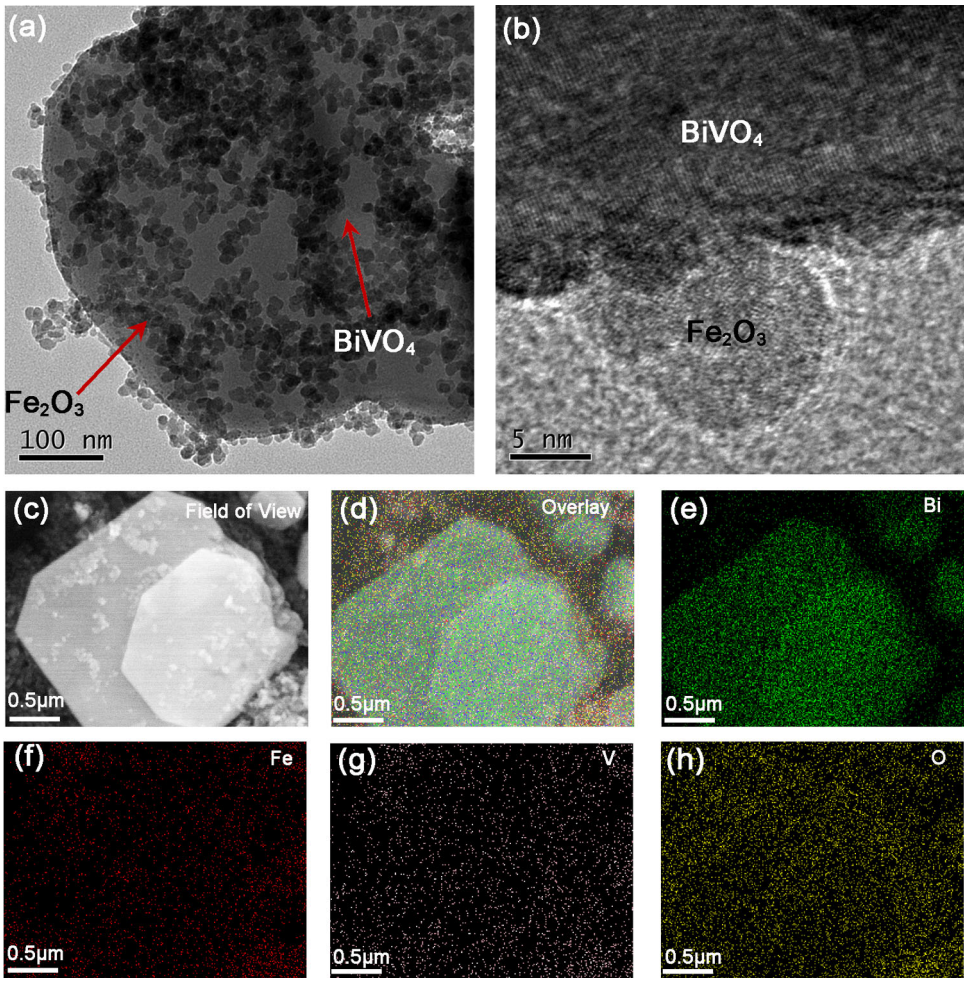

Figure 3 **a** TEM and **b** HRTEM images of FB-1 sample; **c** selected SEM image and **d** the corresponding overlapped elemental mapping image of FB-1; and **e**–**h** elemental mapping images of Bi, Fe, V, and O, respectively. (Green dot: Bi, red dot: Fe, blue dot: V, and yellow dot: O).

respectively [24]. The two characteristic peaks in the high resolution of V 2*p* spectrum shown in Fig. 4d with binding energies of 516.9 and 524.0 eV can be attributed to V2$p_{3/2}$ and V2$p_{1/2}$ for V^{5+} state in FB-1 [25]. The asymmetric O 1s peak shown in Fig. 4e can be ascribed to lattice oxygen with binding energy of 529.8 eV in FB-1 and the physically adsorbed oxygen in the near-surface region [26].

The UV–Vis adsorption spectra of $BiVO_4$ and $Fe_2O_3/BiVO_4$ nanocomposites are shown in Fig. 5a. Compared to the pure $BiVO_4$ nanoplates, the adsorption bands of $Fe_2O_3/BiVO_4$ nanocomposites exhibited a red shift and an enhanced UV–Vis light adsorption, suggesting that the Fe_2O_3 nanoparticle-decorated $BiVO_4$ nanoplates would have high light utilization ability and promoted photocatalytic activity for degradation of dye molecules. In addition, the band gap of the samples was calculated from the plots of $(\alpha hv)^2$ versus photoenergy (hv), and the corresponding estimated band gap values of the $Fe_2O_3/BiVO_4$ nanoplates are between 2.07 and 2.39 eV, which is slightly narrowed in comparison with that of pure $BiVO_4$ (2.44 eV) (Fig. 5b–e) [27].

Photo-Fenton catalytic property and stability of $Fe_2O_3/BiVO_4$ nanocomposites

The photo-Fenton catalytic activity of the $BiVO_4$ and $Fe_2O_3/BiVO_4$ nanocomposites for degradation of MB molecules with the presence of 0.5 mL H_2O_2 is shown in Fig. 6a. The pure $BiVO_4$ nanoplates presented a degradation efficiency of approximately 76.7% for MB after the photo-Fenton reaction time of 40 min. However, the $Fe_2O_3/BiVO_4$-1 (FB-1) nanocomposites showed greatly enhanced photo-Fenton activity, and the degradation ratio of MB reached nearly 100% in 40 min. With the Fe_2O_3 nanoparticles decorated on the surface of $BiVO_4$ increasing from the sample of FB-2 to FB-5, the photo-Fenton catalytic performance decreased. Also, the photo-Fenton catalytic

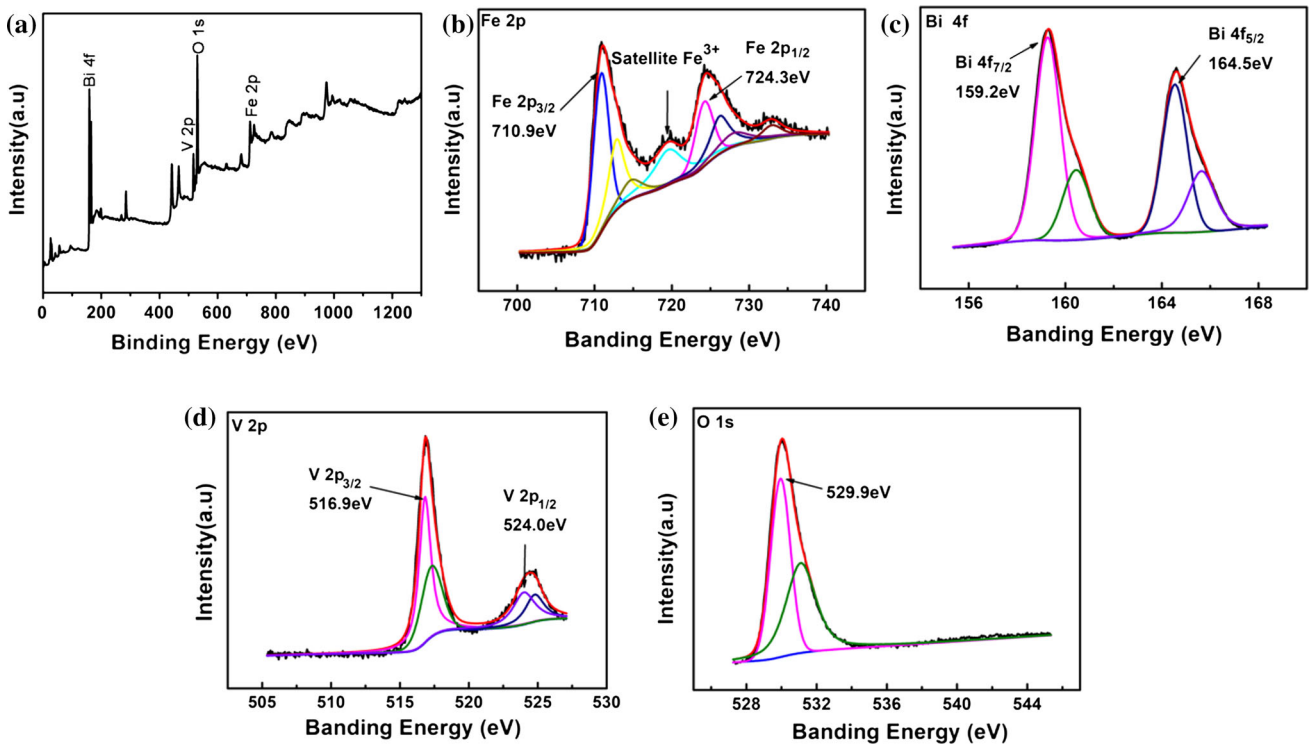

Figure 4 XPS survey spectrum of **a** FB-1 sample and the high-resolution spectra of **b** Fe, **c** Bi, **d** V, and **e** O for FB-1 nanocomposite.

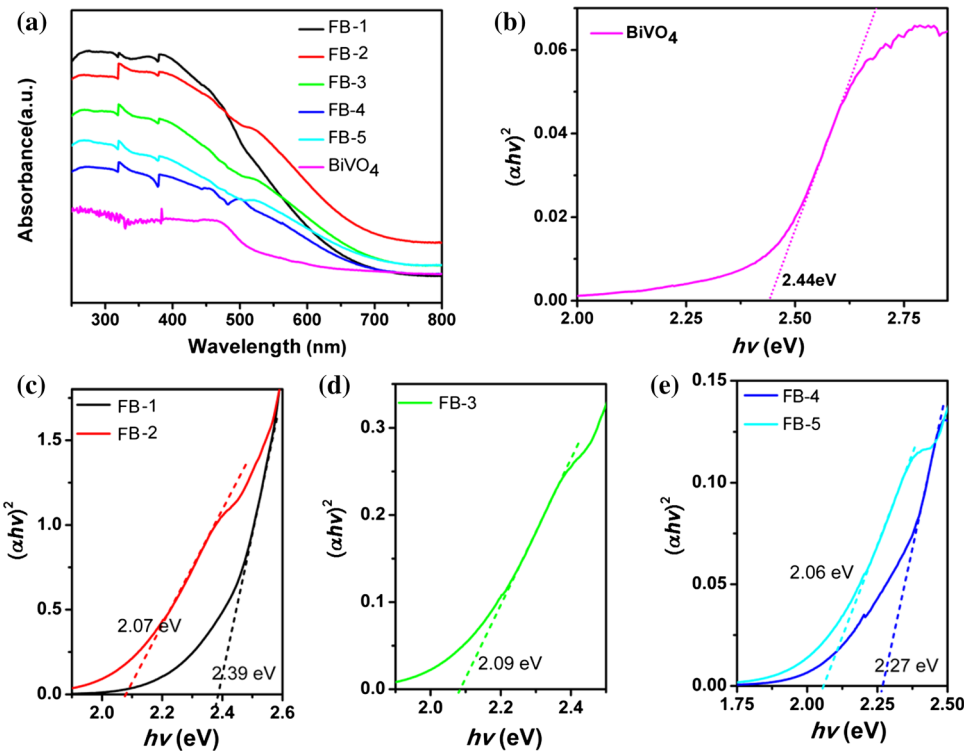

Figure 5 **a** UV–Vis diffuse reflectance spectra of $BiVO_4$ nanoplates and $Fe_2O_3/BiVO_4$ nanoplates with different doping amounts of Fe_2O_3 nanoparticles; corresponding Mott–Schottky plots for **b** $BiVO_4$ nanoplates and **c**–**e** $Fe_2O_3/BiVO_4$ nanoplates.

degradation of MB can be well ascribed to the first-order kinetics (Fig. 6b). The degradation rate constant on FB-1 is approximately 4.7 times to that of pure $BiVO_4$ nanoplates. Series of photo-Fenton degradation experiments were carried out to study the influence of H_2O_2, visible light irradiation, and the

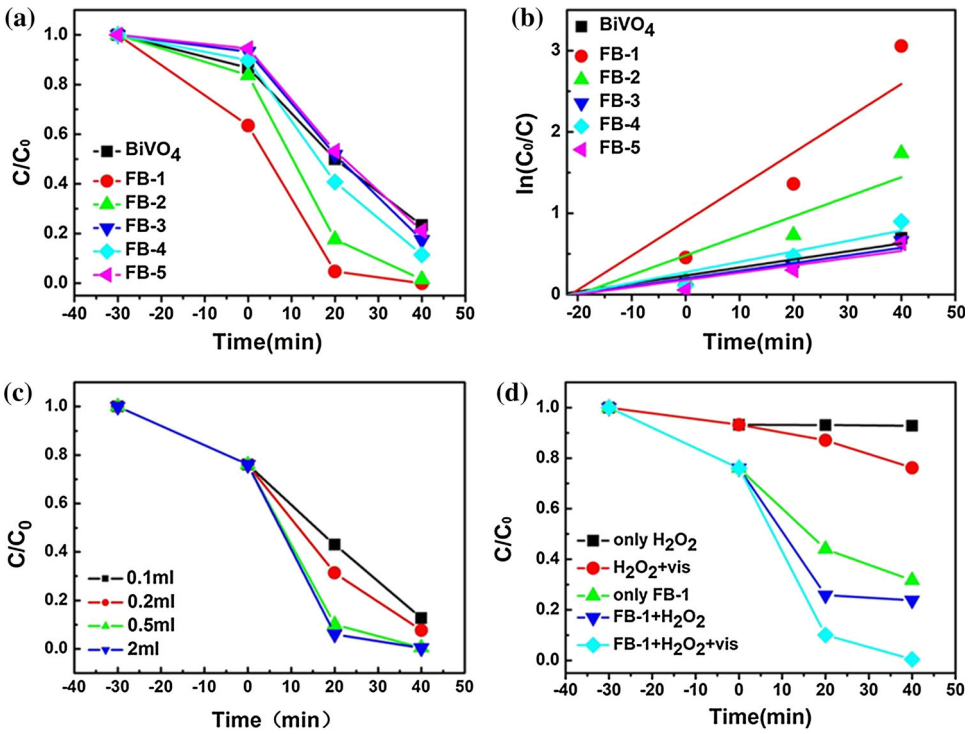

Figure 6 **a** Photo-Fenton catalytic performances of $BiVO_4$ and $Fe_2O_3/BiVO_4$ nanoplates for degradation of MB molecules with the addition of 0.5 mL H_2O_2; **b** kinetics of Fenton degradation of MB dye molecules; **c** effect of H_2O_2 amount on degradation of MB over FB-1 sample; and **d** degradation of MB under different reaction conditions.

$Fe_2O_3/BiVO_4$ catalyst toward MB degradation. As shown in Fig. 6c, the dosage of H_2O_2 played a significant role in the photodegradation reaction, and when the amount of H_2O_2 increased from 0.1 to 0.5 mL, the photo-Fenton degradation efficiency increased from approximately 57.9 to 90.9% in 20 min. However, the degradation of MB did not change too much on further increasing the dosage of H_2O_2 to 2 mL. In addition, more photo-Fenton degradation procedures were implemented to identify the effects of visible light irradiation, H_2O_2, and FB-1 on MB degradation, respectively. As shown in Fig. 6d, if only H_2O_2 was introduced into the reaction system, the dye molecules can hardly be decomposed under visible light irradiation or in the dark, indicating that pure H_2O_2 were unable to efficiently achieve its significant decomposition. The degradation efficiency of MB greatly increased with the presence of $Fe_2O_3/BiVO_4$ nanocomposites no matter whether H_2O_2 is introduced or not in the darkness, revealing that the nanocomposite has catalytic performance for MB dye molecules. When the visible light irradiation was started to the reaction system, the degradation ratio of MB proceeded very fast, illustrating the dominant role of visible light, which can greatly promote the degradation rate.

Furthermore, the photo-Fenton catalytic activity of $Fe_2O_3/BiVO_4$ nanocomposites for degradation of RhB molecules in the presence of 0.2 mL H_2O_2 is carried out and the experimental results are shown in Fig. 7a. The FB-1 nanocomposite also presented the best Fenton catalytic performance. The degradation efficiency toward RhB is approximately 98.4%, which is only about 14.8% over pure $BiVO_4$. The degradation rate constant on FB-1 is more than 15 times to that of pure $BiVO_4$ (Fig. 7b). Figure 7c provides the effect of H_2O_2 dosage for degradation of RhB, and when the dosage of H_2O_2 in the system increased from 0.1 mL to 0.2 mL, the degradation of RhB over FB-1 increased from approximately 37.4% to nearly 100% under 20-min irradiation. Further increasing the amount of H_2O_2 from 0.2 to 2 mL, the degradation efficiency of RhB decreased. It is found that the $^{\cdot}OH$ radicals are the dominant active species in Fenton reaction [28], and the decreasing of hydroxyl radicals in concentration is expected to be the main reason that results in the lowering of degradation efficiency of MB and RhB in the above-discussed experiments. High concentration of H_2O_2 is a scavenger of $^{\cdot}OH$ radicals because the excessive H_2O_2 would capture the free $^{\cdot}OH$ radicals with the formation of H_2O and O_2 based on the equation (Eq. 1) [29]:

$$H_2O_2 + 2^{\cdot}OH \rightarrow 2H_2O + O_2 \quad (1)$$

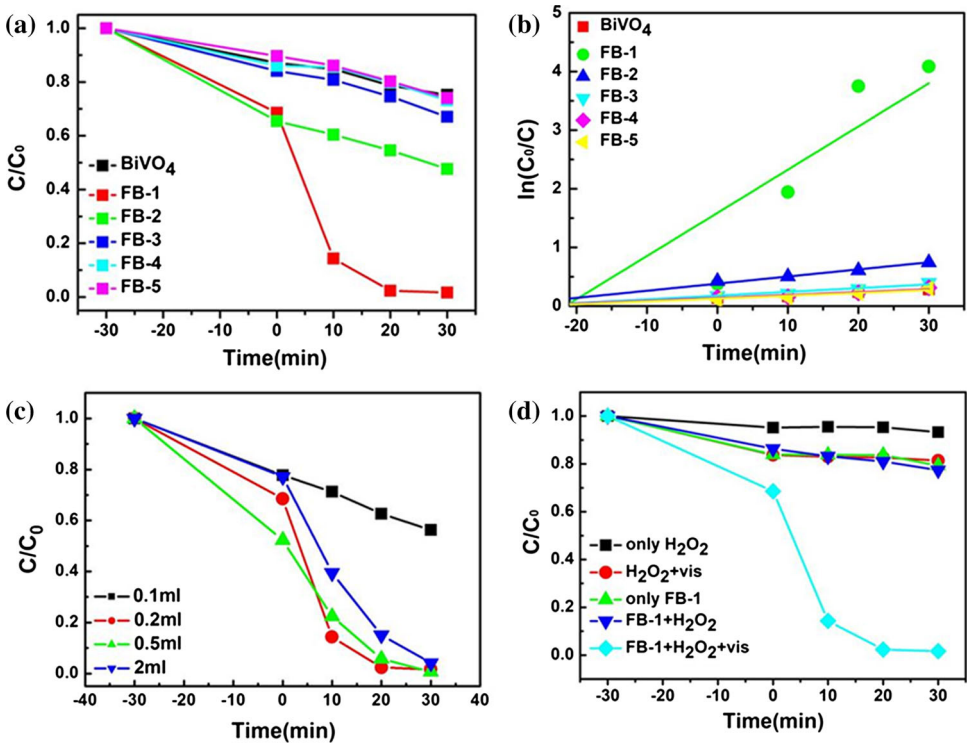

Figure 7 **a** Photo-Fenton catalytic performances of $BiVO_4$ and $Fe_2O_3/BiVO_4$ nanoplates for degradation of RhB molecules with the addition of 0.2 mL H_2O_2; **b** kinetics of Fenton degradation of RhB molecules; **c** effect of H_2O_2 amount on degradation of RhB over FB-1 sample; and **d** degradation of RhB under different reaction conditions.

Figure 7d demonstrates the degradation efficiency of RhB over FB-1 nanocomposites which is greatly increased when appropriate amount of H_2O_2 was introduced under light irradiation. The recycling Fenton reactions were carried out to evaluate the stability and recyclability of the $Fe_2O_3/BiVO_4$ nanocomposites. As shown in Fig. 8, the FB-1 nanocomposite catalysts exhibit excellent recyclability toward degradation of MB (Fig. 8a) and RhB (Fig. 8b), and the degradation efficiency of $Fe_2O_3/BiVO_4$ toward MB and RhB is nearly 100% for the first time of photocatalytic experiment and is still above 85% even after five cycles, in which the slight decrease in degradation efficiency might be caused by the weight loss of catalysts.

Mechanism of photo-Fenton catalytic activity of $Fe_2O_3/BiVO_4$ nanocomposites

The enhanced photocatalytic ability is mainly caused by the generation of highly oxidizing $^{\cdot}OH$ radicals produced in the photo-Fenton reaction, as also reported in the previous Ref. [30]. To further clearly identify the photo-Fenton catalytic mechanism of MB and RhB dye molecules under light irradiation, $^{\cdot}OH$ radicals trapping experiments were carried out by using tert-Butyl alcohol (TBA, 0.005 g) as the scavenger with other conditions unchanged [31]. As shown in Fig. 9a and b, the Fenton degradation of dye molecules is increased with the increase in reaction time. However, after TBA is introduced, the degradation of MB and RhB is significantly suppressed, demonstrating that $^{\cdot}OH$ radicals worked as the main oxidation sources for accelerating the Fenton reaction. Based on the above trapping experimental results, the photo-Fenton degradation mechanism of dye molecules was proposed. Under the irradiation of visible light, only H_2O_2 solution was introduced, and the system showed a limited photocatalytic activity toward dye degradation. However, the degradation rate of dye over $Fe_2O_3/BiVO_4$ catalyst increased significantly when adding both H_2O_2 and visible light irradiation. It is obvious that the $Fe_2O_3/BiVO_4$ nanocomposites can catalytically activate H_2O_2 to produce $^{\cdot}OH$, which can be used for the Fenton reactions. The flat-band potential values of pure Fe_2O_3 and $BiVO_4$ can be obtained from the extrapolation of Mott–Schottky plots reported in Ref. [32, 33], which are approximately − 0.40 V (vs. Ag/AgCl) and − 0.58 V (vs. Ag/AgCl) at pH 7.0, respectively. Because the flat-band potential of the n-type semiconductor is very close to the bottom edge of the conduction band, the redox potential of conduction band of Fe_2O_3 and $BiVO_4$ versus normal

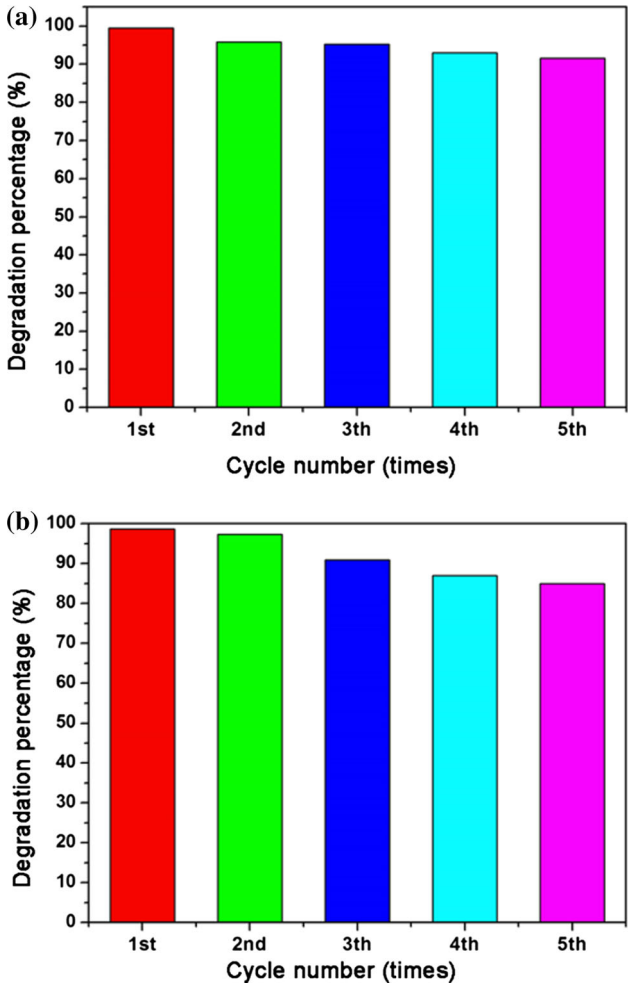

Figure 8 Recycled performance of FB-1 for Fenton catalytic degradation of **a** MB and **b** RhB dye molecules.

hydrogen electrode is calculated to be − 0.16 V and − 0.34 V, respectively. The more negative conduction band and valence band of $BiVO_4$ result in the facile injection of photoinduced electrons from the conduction band of $BiVO_4$ to that of decorated Fe_2O_3 nanoparticles to reduce Fe^{3+}. The reductant Fe^{2+} then reacts with H_2O_2 to form the active $^{\cdot}OH$ radicals, participating in capturing and decomposing the dye molecules. The proposed mechanism can be described by the equations shown as follows:

$$BiVO_4 + hv \rightarrow BiVO_4\left(e^-_{CB} + h^+_{VB}\right) \quad (2)$$

$$Fe^{3+} + e^-_{CB} \rightarrow Fe^{2+} \quad (3)$$

$$H_2O_2 + e^-_{CB} \rightarrow {}^{\cdot}OH + OH^- \quad (4)$$

$$Fe^2 + H_2O_2 \rightarrow Fe^{3+} + {}^{\cdot}OH + OH^- \quad (5)$$

$$\text{MB or RhB} + {}^{\cdot}OH \rightarrow \text{degradation products} \quad (6)$$

Figure 9c shows the proposed process for the photo-Fenton reaction in $Fe/BiVO_4/H_2O_2$/MB or $Fe/BiVO_4/H_2O_2$/RhB system. In the dark environment, MB or RhB dye molecule was firstly adsorbed on the surface of the $Fe_2O_3/BiVO_4$ nanocomposites to reach adsorption equilibrium. Subsequently, under the visible light irradiation, $BiVO_4$ catalyst was excited to generate large amounts of free electron–hole pairs and the electrons were transferred to the surface of catalyst to reduce Fe^{3+} to Fe^{2+} according to Eqs. (2) and (3). As the electron acceptor, H_2O_2 captured the e^-_{CB} to form $^{\cdot}OH$ and OH^- (Eq. 4), and the reduced Fe^{2+} as shown in Eq. (3) further reacted with H_2O_2 to form more $^{\cdot}OH$ radicals (Eq. 5); then, the generated $^{\cdot}OH$ radicals attacked and decomposed the MB or RhB dye molecules to form the final degradation products according to Eq. (6).

Conclusions

In summary, Fe_2O_3 nanoparticles-decorated $BiVO_4$ nanoplates were successfully fabricated as the photo-Fenton reaction platform to demonstrate the synergetic effect of photogenerated electrons and reduction of Fe^{3+} to Fe^{2+} for the improved catalytic activity. The $Fe_2O_3/BiVO_4$ nanocomposite catalysts exhibited efficient photo-Fenton catalytic performance for degradation of MB and RhB dye molecules, which could be attributed to the transformation of the photoinduced electrons from $BiVO_4$ semiconductors to reduce Fe^{3+} to Fe^{2+}, and then, the reductant Fe^{2+} reacts with H_2O_2 to form the active $^{\cdot}OH$ radicals, which captured and decomposed the dyes. Furthermore, the $Fe_2O_3/BiVO_4$ nanocomposites showed superior photo-Fenton catalytic stability on the elimination of dyes, maintaining high activities even after five cycles, and the trapping experiments demonstrated the important roles of active hydroxyl species. Also, the visible light irradiation displays a dominant role in activating the semiconductor-based Fenton catalytic system, which can motivate the $BiVO_4$ photocatalyst to generate free electrons and achieve the recycling of Fe^{3+}/Fe^{2+}, thus enhancing the Fenton catalytic performance of $Fe_2O_3/BiVO_4$ nanocomposites.

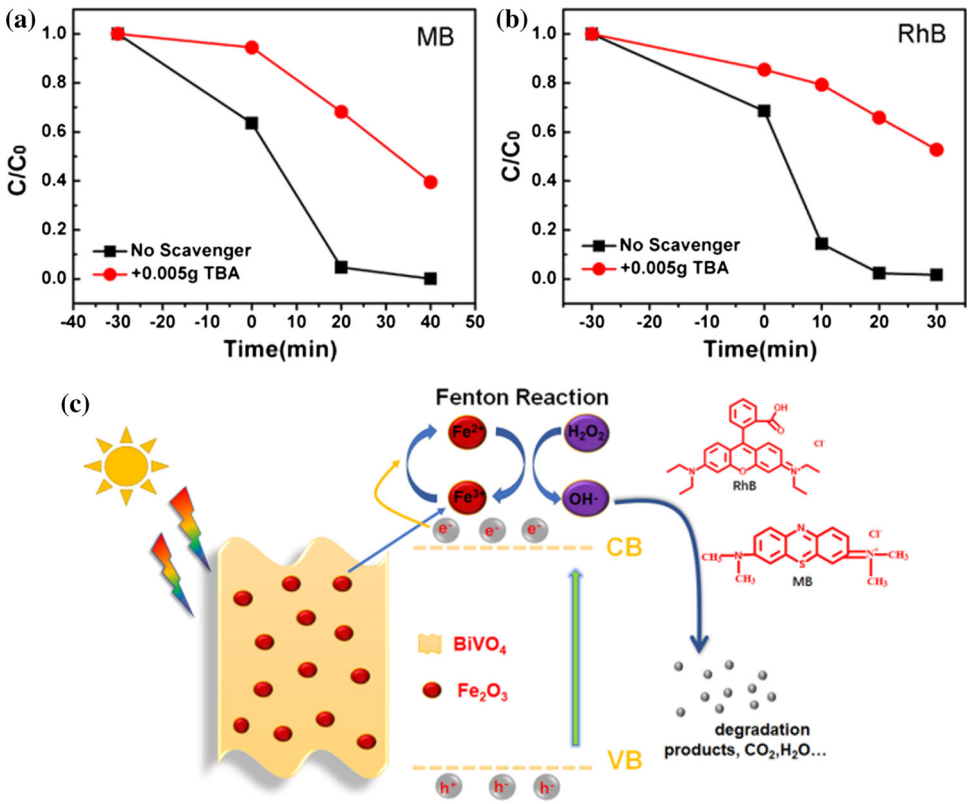

Figure 9 Hydroxyl radical trapping experiments of **a** FB-1/H_2O_2/MB system and **b** FB-1/H_2O_2/RhB system; **c** the photo-Fenton catalytic mechanism for MB and RhB dye molecules over Fe_2O_3/$BiVO_4$ composite.

Acknowledgements

This work was financially supported by the National Natural Science Foundation of China (Grant Nos. 21771031 and 21401018).

References

[1] Clarizia L, Russo D, Di Somma I, Marotta R, Andreozzi R (2017) Homogeneous photo-Fenton processes at near neutral pH: a review. Appl Catal B Environ 209:358–371

[2] Nidheesh PV (2015) Heterogeneous Fenton catalysts for the abatement of organic pollutants from aqueous solution: a review. RSC Adv 5:40552–40577

[3] Yang X, Chen W, Huang J, Zhou Y, Zhu Y, Li C (2015) Rapid degradation of methylene blue in a novel heterogeneous Fe_3O_4–rGO–TiO_2-catalyzed photo-Fenton system. Sci Rep 5:10632

[4] Jiang WL, Xia X, Han JL, Ding YC, Haider MR, Wang AJ (2018) Graphene modified electro-Fenton catalytic membrane for in situ degradation of antibiotic florfenicol. Environ Sci Technol 52:9972–9982

[5] Zhong Y, Yu L, Chen ZF, He H, Ye F, Cheng G, Zhang Q (2017) Microwave-assisted synthesis of Fe_3O_4 nanocrystals with predominantly exposed facets and their heterogeneous UVA/Fenton catalytic activity. ACS Appl Mater Interfaces 9:29203–29212

[6] Navalon S, de Miguel M, Martin R, Alvaro M, Garcia H (2011) Enhancement of the catalytic activity of supported gold nanoparticles for the Fenton reaction by light. J Am Chem Soc 133:2218–2226

[7] Ma J, Xu L, Shen C, Hu C, Liu W, Wen Y (2018) Fe-N-Graphene wrapped Al_2O_3/pentlandite from microalgae: high Fenton catalytic efficiency from enhanced Fe^{3+} reduction. Environ Sci Technol 52:3608–3614

[8] Cheng X, Zu L, Jiang Y, Shi D, Cai X, Ni Y, Lin S, Qin Y (2018) A titanium-based photo-Fenton bifunctional catalyst of mp-MXene/TiO_2-x nanodots for dramatic enhancement of catalytic efficiency in advanced oxidation processes. Chem Commun 54:11622–11625

[9] Li W, Sun T, Li F (2014) Highly efficient Iron nanocatalyst stabilized by double-walled carbon nanotubes and mixed metal oxides for degradation of cationic and anionic dyes by a Fenton-like process. Ind Eng Chem Res 53:18095–18103

[10] Wang Y, Li J, Sun J, Wang Y, Zhao X (2017) Electrospun flexible self-standing Cu-Al_2O_3 fibrous membranes as Fenton catalysts for bisphenol A degradation. J Mater Chem A 5:19151–19158

[11] Khin MM, Nair AS, Babu VJ, Murugan R, Ramakrishna S (2012) A review on nanomaterials for environmental remediation. Energy Environ Sci 5:8075

[12] Dai C, Tian X, Nie Y, Lin HM, Yang C, Han B, Wang Y (2018) Surface facet of $CuFeO_2$ nanocatalyst: a key parameter for H_2O_2 activation in Fenton-like reaction and organic pollutant degradation. Environ Sci Technol 52:6518–6525

[13] Froschl T, Hormann U, Kubiak P, Kucerova G, Pfanzelt M, Weiss CK, Behm RJ, Husing N, Kaiser U, Landfester K, Wohlfahrt-Mehrens M (2012) High surface area crystalline titanium dioxide: potential and limits in electrochemical energy storage and catalysis. Chem Soc Rev 41:5313–5360

[14] Zheng JY, Song G, Hong J, Van TK, Pawar AU, Kim DY, Kim CW, Haider Z, Kang YS (2014) Facile fabrication of WO_3 nanoplates thin films with dominant crystal facet of (002) for water splitting. Cryst Growth Des 14:6057–6066

[15] Shi W, Song S, Zhang H (2013) Hydrothermal synthetic strategies of inorganic semiconducting nanostructures. Chem Soc Rev 42:5714–5743

[16] Saison T, Chemin N, Chanéac C, Durupthy O, Mariey L, Maugé F, Brezová V, Jolivet J-P (2015) New insights into $BiVO_4$ properties as visible light photocatalyst. J Phys Chem C 119:12967–12977

[17] Zhao Y, Li R, Mu L, Li C (2017) Significance of crystal morphology controlling in semiconductor-based photocatalysis: a case study on $BiVO_4$ photocatalyst. Cryst Growth Des 17:2923–2928

[18] Xu T, Zhu R, Zhu G, Zhu J, Liang X, Zhu Y, He H (2017) Mechanisms for the enhanced photo-Fenton activity of ferrihydrite modified with $BiVO_4$ at neutral pH. Appl Catal B Environ 212:50–58

[19] Zhang L, Zhou J, Zhang C (2014) pH-Controlled growth of ultrathin iron vanadium oxide (FeV_3O_8) nanoplatelets with high visible-light photo-catalytic activity. J Mater Chem A 2:14903–14907

[20] Zhao Y, Yao K, Cai Q, Shi Z, Sheng M, Lin H, Shao M (2014) Hydrothermal route to metastable phase FeVO4 ultrathin nanosheets with exposed 010 facets: synthesis, photocatalysis and gas-sensing. Cryst Eng Commun 16:270–276

[21] Li J, Cheng X, Zhang C, Wang J, Dong W, Yang Y, Li Y (2017) Alkalis in iron-based Fischer–Tropsch synthesis catalysts: distribution, migration and promotion. J Chem Technol Biotechnol 92:1472–1480

[22] Alcover IB, David R, Daviero-Minaud S, Filimonov D, Huvé M, Roussel P, Kabbour H, Mentré O (2015) Reversible exsolution of nanometric Fe_2O_3 particles in $BaFe_{2-x}(PO_4)_2$ ($0 \leq x \leq 2/3$): the logic of vacancy ordering in novel metal-depleted two-dimensional lattices. Cryst Growth Des 15:4237–4247

[23] Wei Y, Wang B, Cui X, Muhammad Y, Zhang Y, Huang Z, Li X, Zhao Z, Zhao Z (2018) Highly advanced degradation of thiamethoxam by synergistic chemisorption-catalysis strategy using MIL(Fe)/Fe-SPC composites with ultrasonic irradiation. ACS Appl Mater Interfaces 10:35260–35272

[24] Li X, Cao J, Peng M (2018) The origin of the heterogeneous distribution of bismuth in aluminosilicate laser glasses. J Am Ceram Soc 101:2921–2929

[25] Ranjbar M, Mahdavi SM, Irajizad A (2008) Pulsed laser deposition of W–V–O composite films: preparation, characterization and gasochromic studies. Sol Energy Mater Sol C 92:878–883

[26] Zhang Q, Pang K, Xu Y (2018) Controlled synthesis of Bi_2O_3/BiOBr/Zn_2GeO_4 heterojunction photocatalysts with enhanced photocatalytic activity. J Am Ceram Soc 101:5858–5869

[27] Chen Y, Shi T, Liu P, Ma X, Shui L, Shang C, Chen Z, Wang X, Kempa K, Zhou G (2018) Insights into the mechanism of the enhanced visible-light photocatalytic activity of black phosphorus/$BiVO_4$ heterostructure: a first-principles study. J Mater Chem A 6:19167–19175

[28] Kiwi J, Lopez A, Nadtochenko V (2000) Mechanism and kinetics of the OH-radical intervention during Fenton oxidation in the presence of a significant amount of radical scavenger (Cl^-). Environ Sci Technol 34:2162–2168

[29] Hems RF, Hsieh JS, Slodki MA, Zhou S, Abbatt JPD (2017) Suppression of OH generation from the photo-Fenton reaction in the presence of α-pinene secondary organic aerosol material. Environ Sci Technol Lett 4:439–443

[30] Chala S, Wetchakun K, Phanichphant S, Inceesungvorn B, Wetchakun N (2014) Enhanced visible-light-response photocatalytic degradation of methylene blue on Fe-loaded $BiVO_4$ photocatalyst. J Alloys Compd 597:129–135

[31] Yao Y, Cai Y, Lu F, Qin J, Wei F, Xu C, Wang S (2014) Magnetic $ZnFe_2O_4$–C_3N_4 hybrid for photocatalytic degradation of aqueous organic pollutants by visible light. Ind Eng Chem Res 53:17294–17302

[32] Bi D, Xu Y (2013) Synergism between Fe_2O_3 and WO_3 particles: photocatalytic activity enhancement and reaction mechanism. J Mol Catal A Chem 367:103–107

[33] Hong SJ, Lee S, Jang JS, Lee JS (2011) Heterojunction $BiVO_4$/WO_3 electrodes for enhanced photoactivity of water oxidation. Energy Environ Sci 4:1781–1787

Publisher's Note Springer Nature remains neutral with regard to jurisdictional claims in published maps and institutional affiliations.